



UNIVERSITÀ
DEGLI STUDI
FIRENZE

FLORE

Repository istituzionale dell'Università degli Studi
di Firenze

A Novel 2-D Speckle Tracking Method for High-Frame-Rate Echocardiography

Questa è la Versione finale referata (Post print/Accepted manuscript) della seguente pubblicazione:

Original Citation:

A Novel 2-D Speckle Tracking Method for High-Frame-Rate Echocardiography / Orłowska, Marta; Ramalli, Alessandro; Petrescu, Aniela; Cvijic, Marta; Bezy, Stephanie; Santos, Pedro; Pedrosa, Joao; Voigt, Jens-Uwe; D'hooge, Jan. - In: IEEE TRANSACTIONS ON ULTRASONICS FERROELECTRICS AND FREQUENCY CONTROL. - ISSN 0885-3010. - ELETTRONICO. - 67:(2020), pp. 1764-1775-1775. [10.1109/TUFFC.2020.2985451]

Availability:

This version is available at: 2158/1204508 since: 2020-10-08T14:36:59Z

Published version:

DOI: 10.1109/TUFFC.2020.2985451

Terms of use:

Open Access

La pubblicazione è resa disponibile sotto le norme e i termini della licenza di deposito, secondo quanto stabilito dalla Policy per l'accesso aperto dell'Università degli Studi di Firenze (<https://www.sba.unifi.it/upload/policy-oa-2016-1.pdf>)

Publisher copyright claim:

(Article begins on next page)

A novel 2D speckle tracking method for high frame rate echocardiography

Marta Orlowska, Alessandro Ramalli, Aniela Petrescu, Marta Cvijic, Stéphanie Bézy, Pedro Santos, João Pedrosa, Jens-Uwe Voigt, and Jan D'hooge

Abstract— Speckle tracking echocardiography (STE) is a clinical tool to non-invasively assess regional myocardial function through the quantification of regional motion and deformation. Even if the time resolution of STE can be improved by high frame rate (HFR) imaging, dedicated HFR STE algorithms have to be developed to detect very small inter-frame motions. Therefore, in this paper, we propose a novel 2D STE method, purposely developed for HFR echocardiography. The 2D motion estimator consists of a 2-step algorithm based on 1D cross-correlations to separately estimate the axial and lateral displacement. The method was first optimized and validated on simulated data giving an accuracy of $\sim 3.3\%$ and $\sim 10.5\%$ for the axial and lateral estimates, respectively. Then, it was preliminary tested in-vivo on 10 healthy volunteers showing its clinical applicability and feasibility. Moreover, the extracted clinical markers were in the same range as those reported in literature. Also, the estimated peak global longitudinal strain was compared with that measured with a clinical scanner showing good correlation and negligible differences (-20.94% vs -20.31% , p -value = 0.44). In conclusion, a novel algorithm for STE was developed: the RF signals were preferred for the axial motion estimation, while envelope data for lateral motion. Furthermore, using 2D kernels, even for 1D cross-correlation, makes the method less sensitive to noise.

Index Terms—Speckle tracking, high frame rate imaging, echocardiography, simulation, in-vivo images.

I. INTRODUCTION

Cardiovascular diseases are a major public health problem and their diagnosis relies on a clinical examination that can be challenging. Studies suggest that the assessment of left-ventricular (LV) myocardial function, i.e. the ability of the heart muscle to develop force, for example in patients with suspected heart failure, could lead to more effective diagnosis and treatment [1], [2]. In clinical echocardiography, it is mainly assessed by LV ejection fraction (LVEF). Nevertheless, in the last decade, myocardial deformation imaging, that measures shortening and lengthening of the cardiac muscle throughout the heart cycle, have been introduced to assess regional strain and strain rate [3]–[7]. Among the techniques proposed so far, two have dominated the research arena of echocardiography: Tissue Doppler Imaging (TDI) and Speckle Tracking

Echocardiography (STE). The TDI operates on relatively high frame rates (but on a limited field of view) and uses the phase shift between consecutive echoes to extract the tissue velocity through an auto-correlation algorithm [8], [9]. The estimated values are then displayed in a color overlay on the B-mode image. The major advantage of TDI is that velocity and time interval measurements have excellent temporal resolution and the assessment of peak tissue velocities are sufficiently reproducible. Unfortunately, TDI is angle dependent. Moreover, measured strain and strain rates can be noisy and present artifacts. As such, this approach requires much more experience and can be labor intensive [10]–[13]. On the other hand, STE provides angle-independent strain measurements which are also reasonably accurate [14]. Current STE algorithms are mainly based on: block matching [15]–[17], optical flow [18], [19], and elastic registration [20]–[22]. However, since STE is based on standard B-mode imaging, it operates at low frame rates (FR), typically lower than 80 Hz. Although the mentioned frame rates are sufficient to visualize motion (in real-time), they only describe cardiac kinematics in a very rough way. However, time-dependent parameters, such as velocity and strain rate (SR), require finer time-resolution and, hence, higher frame rates ($>100\text{Hz}$) [23], [24]. Especially, when evaluating patients with higher heart rates or if short-lived events (isovolumetric phase, diastole) need to be tracked, undersampling becomes an issue [13], [23]. For the above reasons, STE is mainly recommended for systolic strain measurements [25], [26].

Lately, advanced imaging techniques have been developed to achieve high frame rates (HFR) and may enable STE to track rapid cardiac events. HFR imaging approaches can be categorized in two groups: those based on focused waves, consisting of the simultaneous transmission of multiple focused beams into different directions [27]–[31]; and those based on the transmission of defocused waves, i.e. diverging or plane waves, together with massive parallel beamforming and coherent compounding in reception [32]–[35]. Nevertheless, since the above-mentioned STE algorithms operate at low frame rates, they cannot be directly applied to HFR imaging as inter-frame motion becomes very small. Therefore, recent studies had reported initial findings on motion estimation on

M. Orlowska was supported by FWO grants No G002617N and G092318N. J.U. Voigt holds a personal FWO research mandate 1832917N. A. Ramalli was supported by the European Union's Horizon 2020 research and innovation programme under the Marie Skłodowska-Curie grant agreement No 786027 (ACOUSTIC project). A. Petrescu was supported by a German Society of Cardiology Research Grant and M. Cvijic by a European Association of Cardiovascular Imaging Research Grant.

M. Orlowska, A. Ramalli, Pedro Santos, João Pedrosa, and J. D'hooge are with the Laboratory of Cardiovascular Imaging and Dynamics, Department of Cardiovascular Sciences, KU Leuven, 3000 Leuven, Belgium.

A. Petrescu, M. Cvijic, S. Bézy, and J.U. Voigt are with Department of Cardiovascular Sciences, University of Leuven, Leuven, Belgium and Department of Cardiovascular Diseases, University Hospitals Leuven, Leuven, Belgium.

HFR data sets. Grondin et al. [36] showed that image compounding of several diverging waves improves image contrast, resolution, and as a result the accuracy of motion estimates. However, these authors did not optimize the settings of the motion estimator for the resulting HFR data sets. Joos et al. [37], by exploiting a motion-compensated HFR scan sequence, presented promising STE results, which were similar to those obtained with clinical scanners. They also focused on the impact that different interpolation functions have on subpixel accuracy of STE. However, which methodology is better used in practice still remains an open point.

In this paper, we made use of DW compounding led by the findings of Grondin et al. However, we went a step further in the sense that we benchmarked the tracking algorithm and tuned it to get optimal performance. Hereto, we propose a novel 2D STE method, purposely developed for HFR echocardiography, based on 1D cross-correlation for both axial and lateral motion estimation. HFR images were obtained by the coherent compounding of images reconstructed from the transmission of 6 diverging waves, as suggested in [36]. The performance of the new approach was optimized by a thorough simulation study. In particular, different kernel sizes were tested and their impact on the accuracy of the estimates was estimated for different signal-to-noise ratio (SNR) levels. Subsequently, the method was tested in-vivo on 10 healthy volunteers. Then, estimated Global Longitudinal Strain (GLS) values were compared to those obtained with a commercial system, while SR clinical markers (i.e. peak values) were compared to the values reported in the literature.

The paper is organized as follows: section II reports the simulation and in-vivo setup and presents the proposed framework and optimization process. Section III shows results obtained for both numeric heart models and in-vivo acquisitions, which are further discussed in section IV. Finally, conclusions are drawn in section V.

II. METHODS

A. Imaging Setup

The same imaging setup was implemented in both simulations and experiments. It was based on the 64-element phased array probe P2-5AC (Samsung Medison, Seoul, South Korea) which has 60% bandwidth centered at 3.5 MHz and a 0.22 mm pitch. The excitation pulse was a single cycle bipolar pulse at 3.5 MHz (duty cycle = 77%) and its amplitude was set to 60 V (for experiments only).

High frame rate imaging was based on the transmission of diverging waves. They were transmitted from 21-element wide sub-apertures. The virtual sources were placed behind the sub-aperture center at $z = -2.42$ mm, thus achieving an aperture angle $2\alpha = 90^\circ$, see Fig. 1. Specifically, each frame was reconstructed using delay-and-sum method as the coherent compounding of the images obtained by the transmission of 6 diverging waves. They were shifted on the x-direction in a triangle transmit sequence and to covered the whole aperture of the array. Hence, the x-coordinates of the virtual sources were $-4.95, -1.21, 2.53, 4.29, 0.55, -3.19$ mm, respectively. This triangle layout was

used to avoid bias in Doppler motion estimates as recommended by Poree et al. [38]. The above transmission scheme was preferred to tilting diverging waves generated by the full aperture since it produced better images, as shown in [39]. Final compounded frames consisted of 144 lines covering a 90° wide sector over a maximum depth up to 13 cm sampled at 25MHz frequency.

B. Simulation Setup

The imaging setup was implemented in Field II [40], [41]. A pulse repetition frequency (PRF) of 5 kHz was used when scanning 3D electromechanical models of the LV from an apical view. These models are available online [42] and provide realistic texture and image features. Every model consists of a 3D cloud of point scatterers, mimicking the local tissue echogenicity by an assigned scattering amplitude. This point cloud is moved according to the electromechanical simulations. However, since the provided positions of the scatterers are sampled at 30 Hz, they were interpolated to 5 kHz using cubic splines for the purpose of this work. One healthy and four ischemic models were considered, corresponding to: a distal and proximal occlusion of the Left Anterior Descending artery (LADdist and LADprox, respectively); an occlusions of the Right Coronary Artery (RCA) and the Left Circumflex (LCX) [42].

The sensitivity of the method to noise was tested with four different SNRs ($+\infty, 20, 15$ and 10 dB) by adding white Gaussian noise to the post-beamformed data. Specifically, since there was no attenuation present in the simulation, SNR was computed on the whole image from the spectral density after filtering both signal and noise. After calculating it within the bandwidth of the transmitted signal, the average SNR was used.

C. In-vivo protocol and setup

Images were acquired by an expert cardiologist in agreement with the protocol approved by the local ethical committee. Briefly, participants signed the consent form and lay supine on the examination bed for a few minutes. Then, blood pressure and heart rhythm were recorded. Apical 4-chamber view

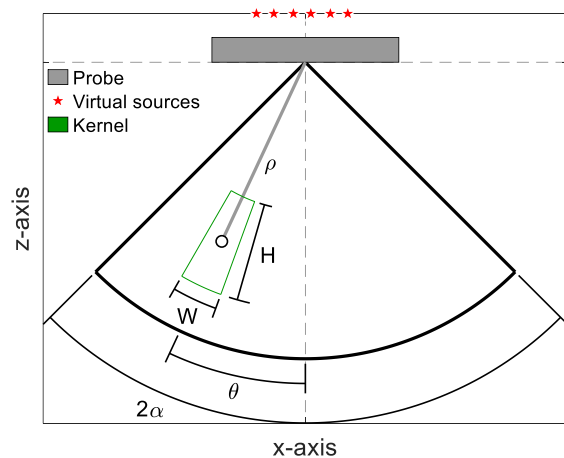


Fig. 1 The reference system and the speckle tracking kernel are defined by the sector scan angle (2α), width (W), height (H) of the kernel as well as radial distance (ρ) and elevation angle (θ).

images were acquired: first, with a reference clinical scanner (Vivid E95, GE Healthcare, Horten, Norway) set in standard cardiac B-mode and connected to phased array probe (M5Sc); then, with the High channel Density Programmable Ultrasound System based on consumer Electronics (HD-PULSE) [43] connected to P2-5AC probe and working in HFR mode, as described in section IIA. To ensure fair comparison between machines, the cardiologist tried to acquire the most similar views with both machines, however some discrepancy might be present. Raw channel data were acquired for 2s and post-processed in Matlab (The MathWorks, Natick, MA), while the data captured with the clinical system was processed in EchoPAC (GE Healthcare, Horten, Norway) in order to extract the reference values of GLS.

The protocol described above was used to scan 10 young, healthy volunteers: 6 men and 4 women with an average age of 29 ± 4 years. Their systolic (119 ± 10 mmHg) and diastolic (64 ± 10 mmHg) blood pressure, heart rate (69 ± 11 bpm) and body mass index (23 ± 2 kg/m²) were in normal range.

D. 2D motion estimator

The 2D motion estimator consists of a 2-step algorithm based on 1D cross-correlations to separately estimate the displacement along and perpendicularly to the beam direction; hereinafter, they will be referred to as axial ($D_{Ax}(\rho, \theta)$) and lateral ($D_{Lat}(\rho, \theta)$) displacement, respectively, where ρ and θ are the probe-to-kernel center distance and its angular position, as shown in Fig. 1.

1) Axial estimation

In the first step, the axial displacement was estimated on the beamformed radiofrequency (RF) signals, as this is known to outperform tracking of the envelope data [44]. 1D cross-correlation was computed between kernels, W_{Ax} wide and H_{Ax} high, at the same position on consecutive frames. Given that the displacement at HFR can be small, the cross-correlation was interpolated, through a 10:1 spline algorithm, enabling subsample motion estimation. The position of the maximum was then used to calculate the axial displacement that was assigned to the pixel at the center of the investigated kernel. The displacement was calculated for the whole imaging plane by moving the kernels with an axial overlap of 80% and a lateral shift of 1 line. Finally, to obtain an estimate for every pixel of the RF frame, sample-based re-correlation was used, as described in [44]. In brief, a spline was fit through displacement estimates obtained from adjacent kernels to up-sample the estimated field along the axial direction.

2) Lateral estimation

In the second step, the lateral displacement was estimated on the envelope data. Hereto, the 1D cross-correlation was computed between kernels, W_{Lat} wide and H_{Lat} high. However, due to the low lateral resolution and the small lateral inter-frame motion at HFR, lateral motion cannot be estimated between consecutive frames. Hence, the displacement of the j -th estimation point ($D_T(\rho_j(i), \theta_j(i))$) was computed between frames with longer time gap (T), i.e. the i -th frame was compared with the frame with index $i+T \cdot FR$. Then, the displacement of the i -th frame was defined as:

$$D_{Lat} \left(\rho_j \left(i + \frac{T \cdot FR}{2} \right), \theta_j \left(i + \frac{T \cdot FR}{2} \right) \right) = \frac{D_T(\rho_j(i), \theta_j(i))}{T}. \quad (1)$$

In contrast to the first step, the axial position of the kernel on the reference frame ($\rho_R(i)$) and on the search frame ($\rho_S(i + T \cdot FR)$) was not the same, but was shifted in the axial direction based on the estimation at previous step, i.e.:

$$\rho_S(i + T \cdot FR) = \rho_R(i) + \sum_{k=i}^{i+T \cdot FR-1} D_{Ax}(\rho(k), \theta). \quad (2)$$

It ensures that the kernel extracted from the first frame is still visible in the frame where the search is conducted, despite of T .

Spline interpolation for subsample motion estimation was done in the same way as for axial estimation, as well as interpolation to obtain a dense motion field, where estimates on the same scanning line were connected using spline to up-sample the estimated field.

E. Accuracy estimation

Displacement estimates were benchmarked against the reference displacement, which was extracted from the position of the scatterers on the heart models and projected from model coordinates (x, y, z) to imaging plane coordinates (ρ, θ).

The accuracy of the 2D motion estimator was evaluated separately for axial (ϵ_{Ax}) and lateral (ϵ_{Lat}) displacement by calculating the average root-mean-square error as follows:

$$\epsilon_d = \frac{1}{N} \sum_{j=1}^N \sqrt{\frac{\frac{1}{M} \sum_{i=1}^M (R_d(\rho_j(i), \theta_j(i)) - D_d(\rho_j(i), \theta_j(i)))^2}{\max_i(|R_d(\rho_j, \theta_j)|)}}} \quad (3)$$

where the subscript d is Ax or Lat whether the error is assessed for axial or lateral displacement respectively. R is the reference displacement frame, M is the total number of frames and N is the number of error estimation points selected on the myocardial wall. Indeed, even if the displacement was estimated for all pixels in the frame, the accuracy was assessed in a subset of $N=101$ points. Specifically, the initial position of the j -th estimation point ($\rho_j(1), \theta_j(1)$) was determined through a semi-automatic segmentation that exploits B-Spline Explicit Active Surfaces (BEAS) [45]. It automatically extracts the position of both endocardial and epicardial borders on the end-diastolic frame, which may be manually corrected if required. Then, the 101 error estimation points were selected on the central line in the middle between the endocardial and epicardial borders at uniform distances from each other (~ 2 mm). Finally, the estimation points were tracked throughout the heart cycle and their position on the i -th frame was calculated as:

$$\rho_j(i) = \rho_j(i-1) + R_{Ax}(\rho_j(i), \theta_j(i)), \quad (4)$$

$$\theta_j(i) = \theta_j(i-1) + R_{Lat}(\rho_j(i), \theta_j(i)). \quad (5)$$

F. Optimization

In order to find the optimum settings for the proposed displacement estimator, ϵ_{Ax} and ϵ_{Lat} were assessed for different

kernel sizes (H_{Ax} , W_{Ax} , H_{Lat} , W_{Lat}) and T values on the images obtained for the healthy heart model.

First, ϵ_{Ax} was calculated for $W_{Ax}=1$ line and H_{Ax} ranging from 0.5 to 12 mm to find $\overline{H_{Ax}}$, i.e. the optimal value of H_{Ax} . Then, ϵ_{Ax} was computed for $H_{Ax}=\overline{H_{Ax}}$ and W_{Ax} ranging from 1 to 35 lines to find $\overline{W_{Ax}}$, i.e. the optimal value of W_{Ax} .

On the other hand, the optimization of the ϵ_{Lat} required testing three parameters: H_{Lat} , W_{Lat} and T. First, ϵ_{Lat} was calculated for $H_{Lat}=1$ pixel, $T=24$ ms and W_{Lat} ranging from 5 to 50 lines. After the optimal W_{Lat} ($\overline{W_{Lat}}$) was found, ϵ_{Lat} was assessed with $W_{Lat}=\overline{W_{Lat}}$, $T=24$ ms and different H_{Lat} (1-10 mm). Finally, T values ranging from 10 to 50 ms were tested with the optimal $H_{Lat}=\overline{H_{Lat}}$ and $W_{Lat}=\overline{W_{Lat}}$ to find \overline{T} , i.e. the optimal T value.

After the optimization, the 2D motion estimator with optimal parameters ($\overline{H_{Ax}}$, $\overline{W_{Ax}}$, $\overline{H_{Lat}}$, $\overline{W_{Lat}}$ and \overline{T}) was applied on the 4 diseased heart models to validate the method.

G. In-vivo validation

1) Spatial filtering

Although the motion estimation is performed for the whole frame, only a subset of points (determined through BEAS) was of interest. As those points were tracked independently, this could result in an unnatural motion of the contour. To avoid this issue, the positions of the tracked points were connected by a spline line, which was smoothed by a Savitzky-Golay filter [46]. It minimizes the least-squares error in fitting a polynomial to windows of noisy data. For the purpose of this work a 2nd order polynomial and an 11-point wide window was used. Specifically, the contour was spatially smoothed during the tracking process for each point of estimation and the position of the tracked points updated accordingly.

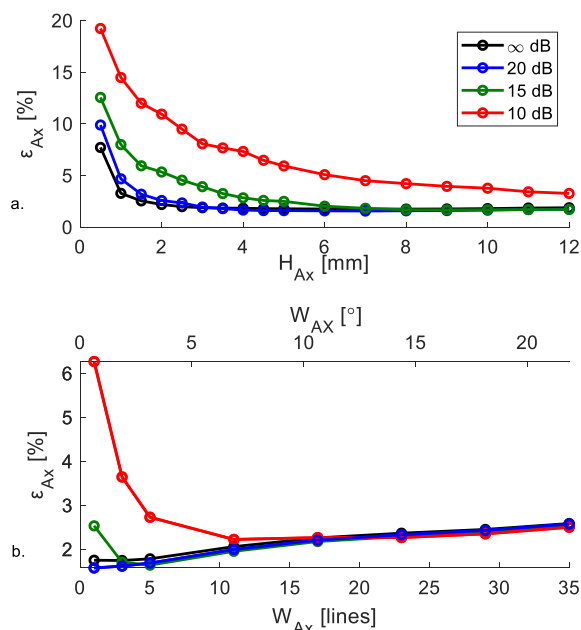


Fig. 3 The estimation error ϵ_{Ax} for different kernel heights (a) and widths (b). The kernel width (W_{Ax}) was set to 1 line in (a), while the kernel height (H_{Ax}) was set to 4.5 mm in (b).

2) Strain and Strain Rate

The myocardial tracking contour was divided into six segments according to the recommended guidelines of the European Association of Cardiovascular Imaging (EACVI) / American Society of Echocardiography (ASE) [23]. For each segment, strain, which is defined as the deformation of a contour, was calculated as follows:

$$S(t) = \frac{L(t) - L_0}{L_0}$$

where $L(t)$ is the length of the contour at time instance t and L_0 is its initial length, i.e. at end-diastole. Moreover, the speed at which deformation occurred (i.e. strain rate) was computed as:

$$Sr(t) = \frac{L'(t)}{L(t)}$$

with $L'(t)$ the speed of deformation and $L(t)$ the instantaneous length of the contour [24].

To compute global strain and strain rate curves each segment was labeled, based on the expertise of a cardiologist by visual readings, as 'tracked' or 'non-tracked'. The latter segments were excluded from further analysis, the former ones were used to calculate the global strain and strain rate curves as a mean curve. Finally, clinical markers, i.e. systolic, early and late diastolic peak values, were compared with those in the literature and the systolic peak of the GLS curve was compared with the value extracted using the GE Vivid E95.

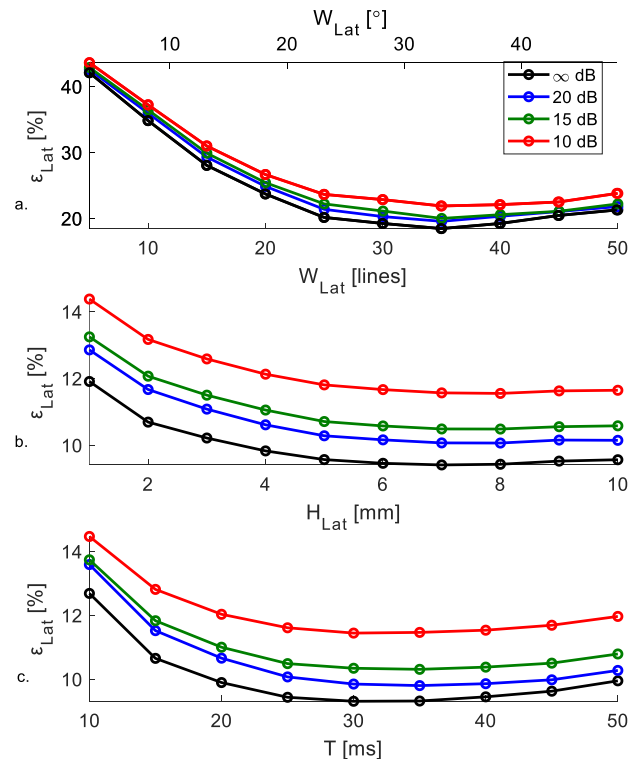


Fig. 2 The estimation error ϵ_{Lat} for different kernel widths (a), heights (b) and time-gaps (c). The kernel height (H_{Lat}) was set to 1 pixel and time-gap (T) to 24ms in (a), while the kernel width (W_{Lat}) was set to 35 lines and $T = 24$ ms in (b). In (c), Kernel size was set to $W_{Lat} = 35$ lines, $H_{Lat} = 7$ mm.

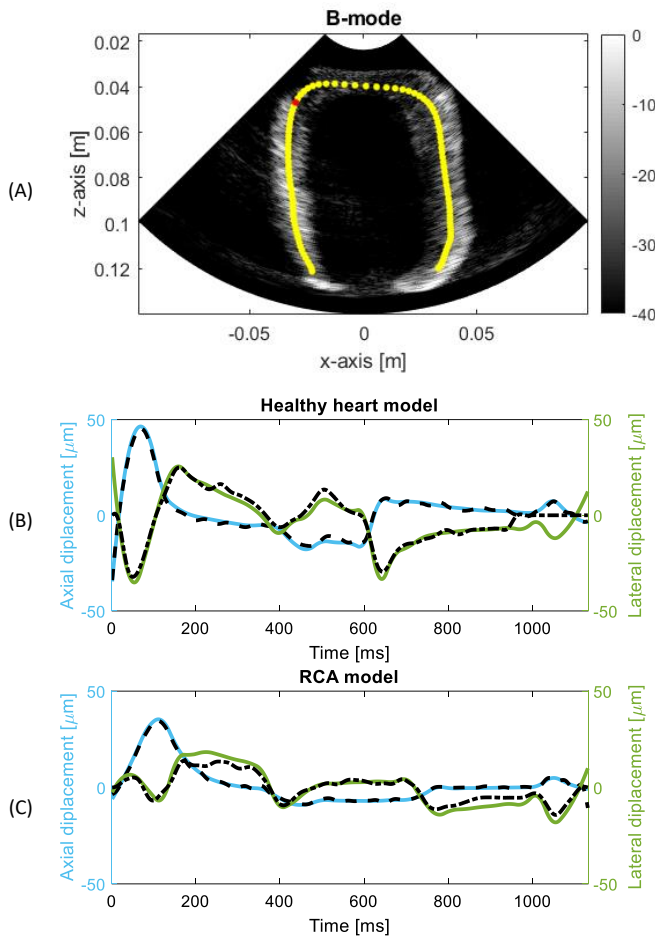


Fig. 5 (A) Example B-mode image of a simulated heart and the related contour (yellow dots) used for the estimation of the method accuracy. (B) and (C): Examples of displacement curves obtained for the estimation point in apical region, highlighted as a red dot on the top image. (B) was computed for the healthy heart model, while (C) for the RCA one. The reference axial and lateral displacements are drawn in blue and green, respectively, while black dashed lines were obtained with the proposed estimator.

III. RESULTS

A. Axial estimation

Fig. 2a shows ϵ_{Ax} for different SNRs as a function of the kernel height (H_{Ax}). As expected, the accuracy of the estimates is affected by SNR, with higher ϵ_{Ax} for lower SNRs.

Septum	Basal	100%
	Mid	100%
	Apical	40%
Lateral	Basal	50%
	Mid	70%
	Apical	0%

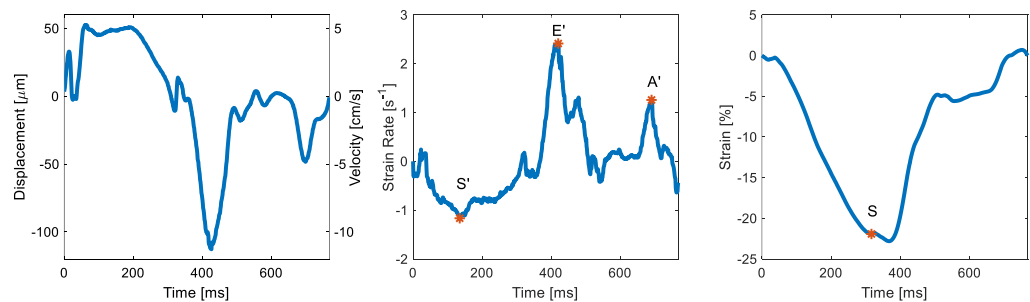


Fig. 4 An example of global displacement (left), strain rate (middle) and strain (right) curves from an in-vivo recording. Early systolic (S'), early (E') and late (A') diastolic peaks are highlighted on the strain rate curve, while the end systolic peak (S) is highlighted on the strain curve.

TABLE II ϵ_{Ax} , ϵ_{Lat} , ϵ_{Strain} , ϵ_{SR} FOR DIFFERENT SNRS.

	SNR (dB)				Average
	$+\infty$	20	15	10	
ϵ_{Ax} (%)	2.1	2.0	2.0	2.2	2.1
ϵ_{Lat} (%)	9.3	9.9	10.3	11.4	10.2
ϵ_{Strain} (%)	3.9	3.8	4.0	4.8	4.1
ϵ_{SR} (%)	6.0	6.0	6.2	6.6	6.2

TABLE III ϵ_{Ax} , ϵ_{Lat} , ϵ_{Strain} , ϵ_{SR} FOR DIFFERENT MODELS.

	Healthy	LADdist	LADprox	LCX	RCA	Average
ϵ_{Ax} (%)	2.1	3.6	3.9	3.7	3.2	3.3
ϵ_{Lat} (%)	9.3	10.0	9.1	10.0	14.1	10.5
ϵ_{Strain} (%)	3.9	13.3	12.2	6.3	3.0	7.7
ϵ_{SR} (%)	6.0	6.4	5.8	5.1	6.2	5.9

Qualitatively, all the plots approximately present an exponential decay pattern, where the decay rate is increasing with the SNR level. Higher H_{Ax} resulted in lower ϵ_{Ax} . However, since higher H_{Ax} implies worse spatial resolution, a compromise has to be made in order to choose $\overline{H_{Ax}}$. Specifically, we arbitrarily set a 5% threshold on the difference in ϵ_{Ax} between the best (SNR= $+\infty$ dB) and the worst (SNR=10dB) case. Doing so, $\overline{H_{Ax}}$ was 4.5 mm.

Fig. 2b shows ϵ_{Ax} for different SNR levels, with $H_{Ax} = \overline{H_{Ax}} = 4.5$ mm as a function of W_{Ax} . For the recording without noise and SNR = 20dB, the error slightly increases (<1%) for wider kernels. However, for the recording with SNR=10dB, ϵ_{Ax} decreases significantly with kernel width, showing a minimum value of 2.2% for $W_{Ax} = 11$ lines (7°) which is comparable to the value obtained with SNR= $+\infty$ dB (2.1%). Hence, $\overline{W_{Ax}}$ was chosen to be equal to 11 lines (7°).

B. Lateral estimation

In Fig. 3a the influence of kernel width (W_{Lat}) on ϵ_{Lat} for different SNR levels is presented. Again, as expected, the accuracy of the estimates is affected by SNR with ϵ_{Lat} higher for lower SNRs. Qualitatively, all the plots present a similar pattern with a clear minimum for $W_{Lat} = 35$ lines (22°) for all SNR levels where ϵ_{Lat} ranges from 18.5% to 21.9%. $\overline{W_{Lat}}$ was chosen to be 35 lines (22°).

Fig. 3b illustrates the estimation accuracy as a function of the kernel height for different SNR levels. All noise levels obtained

a similar pattern with the minimum error ranging from 9.4% to 11.6% for $H_{Lat} = 7\text{mm}$. Hence, $\overline{H_{Lat}}$ was chosen to be 7 mm.

The effect of time-gap (T) on the estimation error is shown in Fig. 3c. As observed in previous tests, all plots again present a similar pattern. The minimal ϵ_{Lat} is obtained for $\overline{T}=30\text{ms}$, giving an error from 9.3% to 11.5%.

C. Validation


Error values (ϵ_{Ax} , ϵ_{Lat} , ϵ_{Strain} , ϵ_{SR}) were obtained by using the optimal parameters determined above. Examples of estimated axial and lateral displacement curves for the point in the apical region for the healthy heart model and for the RCA one are shown in Fig. 4. Similar curves were obtained for other points. Anyway, in general, estimated curves follow closely the reference ones, resulting in $\epsilon_{Ax}=2.1\%$ and $\epsilon_{Lat}=9.3\%$.

Table I reports ϵ_{Ax} , ϵ_{Lat} , ϵ_{Strain} and ϵ_{SR} obtained for different SNRs. The displacements are more accurately estimated in the axial direction than in the lateral. Moreover, ϵ_{Ax} is fairly stable across noise levels with a difference lower than 0.2% between the two extreme cases. On the other hand, ϵ_{Lat} showed to be more sensitive, but the difference between best and worst scenario remained small (2.1%). Strain and strain rate are relatively stable across noise levels till SNR = 15dB. Then, the error slightly increases (<1%) with SNR = 10dB. Nonetheless, the estimated motion gives in average $\epsilon_{Strain}=4.1\%$ for strain and $\epsilon_{SR}=6.2\%$ for strain rate.

In Table II, errors are reported for all 5 models. It can be observed that ϵ_{Ax} is slightly higher (~1.5%) than for the healthy heart model, whereas ϵ_{Lat} is relatively steady (~9.6%) with the RCA model as an exception (14.1%), where slightly higher discrepancies in the apical region were shown (Fig. 4). ϵ_{SR} is fairly stable between models giving in average 5.9%. ϵ_{Strain} fluctuates more and the difference between best and worst scenario is 10.3%. Higher errors are obtained for those models

where a bigger area is affected by the specific disease, limiting the movement of the diseased segments and the segmental strain. Hence, even a small difference between estimated and reference values gives higher relative errors. However, the obtained error in average is still relatively small (7.7%).

D. In-vivo cardiac images

Table III shows the tracking feasibility, i.e. the percentage of segments (illustrated in Fig. 6) labeled as “tracked” by an expert reader. The best feasibility was obtained for the mid and basal parts of the septum (i.e. 100%). For the same regions in the lateral wall, the performance of the algorithm was lower (~60% on average). Unfortunately, the tracking of apical segments was not sufficient in both the septal and lateral walls (40% and 0%, respectively) due to strong artifacts in those areas. As a qualitative example, Fig. 6 shows a frame extracted from the accompanying clip  of the in-vivo tracking of a healthy volunteer. The tracked contour can be seen overlaid on the B-mode images. Moreover, the segmental strains are displayed and colored the same way as the respective segments in the contour; dotted lines correspond to the segment with 0% feasibility, i.e. the apical lateral wall. It can be observed that in-vivo images present low SNR, strong near field clutter, and the hardware switching noise pattern in the middle of the B-mode that can influence the estimation around the apex. Finally, since a phased array was used, resolution decreases along depth, which makes speckles more coarse and more difficult to track. In general, since the quality of the images depends on the specific point of interest, it might differently influence the behavior of the speckle tracking algorithm for different points of interest according to their position in the image.

Qualitatively, the “tracked” segments gave curves with a physiological pattern. They presented typical trends of conventional strain and strain rates traces: the latter ones show

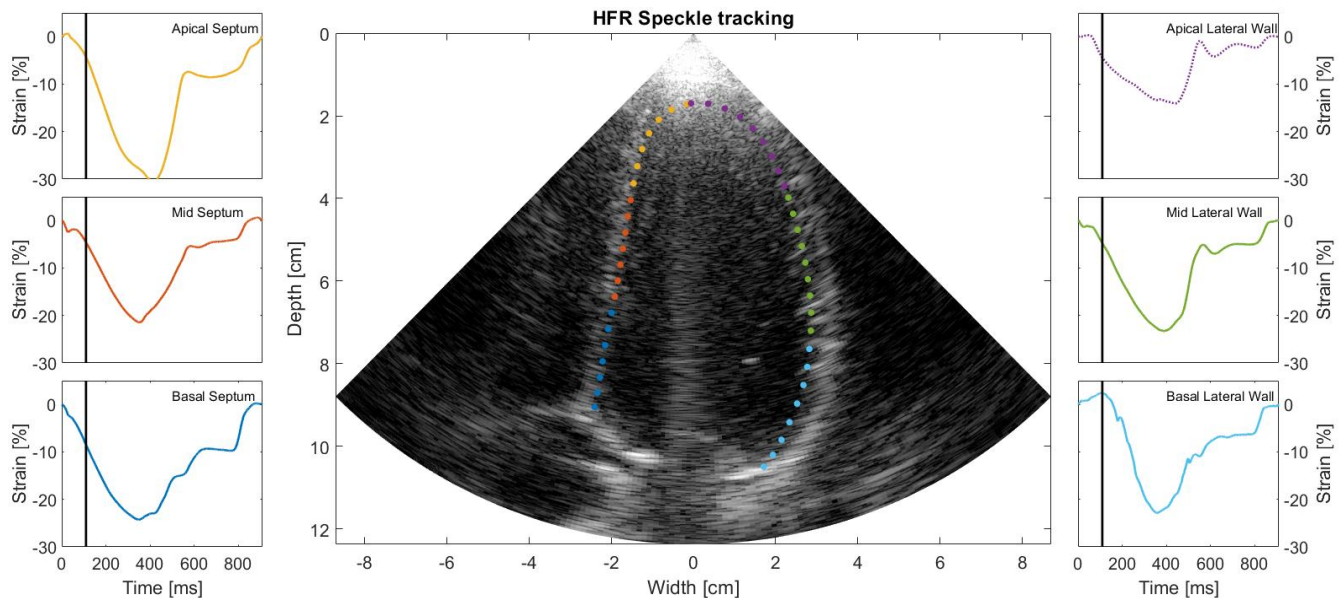


Fig. 6 A frame extracted from the accompanying clip of the in-vivo tracking of a healthy volunteer. In the center, the tracked contour (colored dots) can be seen overlaid on the B-mode image. The segmental strains for the septum (left panels) and lateral wall (right panels) are displayed and colored the same way as the respective segments in the contour; the dotted line of the apical lateral wall highlights 0% feasibility. In those panels, the black line at 100ms indicates the time instant at which the B-mode image corresponds. A noisy pattern in the middle of B-mode along the depth is a switching noise caused by hardware.

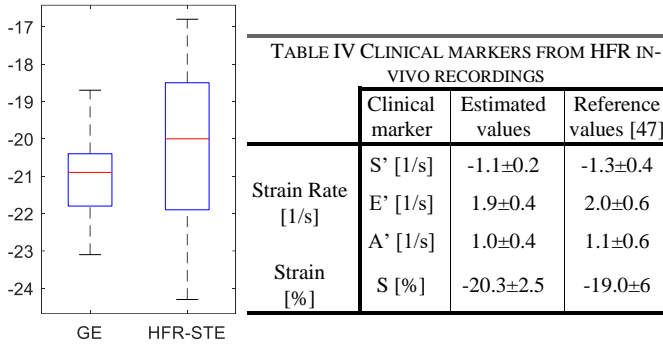


Fig. 7 Comparison between GLS peak values for 10 healthy volunteers obtained with the GE scanner and the proposed method (HFR-STE).

clear systolic (S'), early (E') and late (A') diastolic peaks, while the former ones show a clear end systolic peak (S). As an example, the global strain rate and strain traces extracted from an in-vivo recording are shown in Fig. 5. Similar results were obtained for other recordings. Moreover, the clinical markers extracted for the segments labeled as "tracked" were in the same range as those reported in [47], as shown in Table IV.

Fig. 7 shows the comparison between the global peak systolic strain values obtained with the proposed method and those obtained with the GE Vivid E95 scanner. Paired-sample t-test was performed and the average values were found not significantly different between the two approaches ($-20.94 \pm 1.24\%$ for GE vs $-20.31 \pm 2.46\%$ for HFE-STE, p -value = 0.44), although it can be noticed that a wider range was obtained in the HFR recordings. Furthermore, comparing the GLS values obtained with the proposed HFR STE method with those obtained with the GE solution, the Bland-Altman statistics gave $0.7\% \pm 5\%$ (mean difference ± 2 std).

IV. DISCUSSION

In this paper, a novel speckle tracking algorithm for high frame rate imaging was introduced. First, the method was optimized, considering different noise levels, by using ultrasound simulations based on the 3D electromechanical model of a healthy LV. Then, it was validated by different diseased models. Finally, the algorithm was tested in-vivo on 10 healthy volunteers.

The algorithm estimates the displacement among frames in two steps: first, the axial displacement is computed from the RF signals; then, the lateral displacement is assessed from envelope signals. The RF signals were preferred for the axial estimation since they are more sensitive to the small displacements, with an improved accuracy of roughly 20% at HFRs. Moreover, the RF-based tracking algorithm performed similarly for different frame rates, while the accuracy of the envelope-based algorithm improved for lower frame rates, although the error was still higher than the RF-based method. Those findings, which confirmed previous studies [48], were not shown in this paper for the sake of brevity.

However, this does not hold for detecting the motion perpendicular to the beam. Indeed, the worse resolution achieved in the lateral direction jeopardizes the possibility to detect small displacements [49], hence envelope data was

preferred since bigger displacements were detected on frames with longer time lags.

Simulation results showed, as expected, that noise worsened the accuracy of the displacement estimates (Fig. 2a and Fig. 3a). However, the use of 2D kernels, even with 1D cross-correlation, made the estimations less susceptible to SNR, as shown in Fig. 2b and Fig. 3b. Moreover, the accuracy of the axial estimates was better than that of the lateral ones giving average errors $\epsilon_{Ax} \approx 2.1\%$ and $\epsilon_{Lat} \approx 10.2\%$, respectively, see Table I. Again, this can be attributed to the worse lateral resolution compared to the axial one. In addition, since the lateral resolution worsens for increasing depth, the deeper speckles are smeared in the lateral direction, making tracking even more challenging. Moreover, strain and SR don't change much ($<1\%$) across the noise levels giving in average $\epsilon_{SR} = 5.9\%$ and $\epsilon_{Strain} = 10.3\%$.

It is noteworthy that a different order of optimization could give different optimal values. This is a known problem of optimization method with multiple parameters. However, a small test was performed where after choosing optimal H_{Lat} , optimization of W_{Lat} was rerun, but this time with H_{Lat} equal to 7mm and it gave the same optimal $W_{Lat} = 35$ lines. Similar behavior of the optimization curve was also observed when different (diseased) models were used.

After optimizing the method, using the model of a healthy heart, the motion of 4 diseased heart models was estimated. It was observed that both ϵ_{Ax} and ϵ_{Lat} were only slightly affected by abnormal wall movements (Table II). Especially, worse ϵ_{Ax} and ϵ_{Lat} were observed in the apical region where the motion was more complex (see Fig. 4). Afterwards, the results were used to perform 2-way Anova (not shown for sake of brevity) to examine the influence of: 1) model and segment to understand the effect of motion complexity and position within the image respectively; 2) noise and segment to similarly get insight in the effect of noise and segment position. It showed that the axial estimates were significantly influenced by the motion complexity and spatial position, while the lateral estimates were influenced by noise.

Finally, in-vivo tests were performed. The clip (Fig. 6 shows an extracted frame) shows that the mid part of both walls can be easily tracked where the lateral resolution is good and no artifacts are visible. Basal parts are slightly more challenging most likely due to the worse lateral resolution. However, the most difficult to track segments are the apical ones. Here, even though the lateral resolution is better than for mid segments, the near field clutter is very intense, and the myocardium is barely visible.

Feasibility was assessed by an expert cardiologist and was higher for the segments on the septum and lower for those on the lateral wall. Mainly, this was due to image quality which is known to be worse – on average – in the lateral wall [50]. Nevertheless, for the properly tracked segments, the strain and strain rate curves had a physiological pattern with values comparable to those in the literature, as shown in Table IV. Although the feasibility was evaluated on segmental level, only global results were compared with those of the clinical scanner since previous studies showed that segmental longitudinal strain measurements suffer from a high variability. Specifically, in [51], it was concluded that single segmental strain values

should be used with caution in the clinic since the reliability of different software packages to follow segmental function varies considerably.

The GLS comparison with the GE Vivid E95 gave similar average values. The slightly different values could be partially ascribed to the difficulty in finding the exact same views with both scanners, since the cardiologist had to switch probe during acquisition. Also, larger variances for the proposed approach (Fig. 7) were expected which could be due to overall lower image quality in HFR imaging sequence running on the research scanner.

It is worth highlighting that, even if the results presented in the simulation study gave satisfactory accuracies both in the axial and lateral direction and for the different segments, it was observed that the in-vivo feasibility on the apical region was very low. This is likely due to the high intensity artifacts that comes from e.g. ribs, multiple reflections and near field reverberations [52]. Unfortunately, those kind of artifacts were not simulated so the effect of clutter could not be assessed and benchmarked on the tracking algorithm accordingly. However, this implies the simulation to take into account nonlinearity, acoustic heterogeneities, and power law absorption, e.g. by implementing more advanced time-domain model of acoustic wave propagation as implemented in e.g. the k-Wave toolbox [53]. Alternatively, since generating realistic acoustic clutter in synthetic models is far from trivial and was thus not feasible in the context of this study, clutter filtering could be used in a future study.

Another limitation of the proposed optimization is that the kernel size was kept the same for different parts of the image although different challenges (artifacts, distance between lines) could impact on the accuracy of the estimates depending on the depth of interest. Hence, an advanced optimization of the kernel size could be conducted to optimize the method for the different wall segments, especially if other surrounding structures would be included in the model.

A final comment should be made on the frame rate required for a time resolved description of strain and strain rate curves. Hence, since HFR imaging (~ 957 Hz) allowed computing spectra on a wide range of frequencies, the spectra of strain rate curves obtained with the proposed method were compared to those obtained at low frame rate (~ 72 Hz) with the commercial scanner (Fig. 8). Specifically, the spectra were obtained as the

average spectrum from different segments and volunteers. Clearly, Fig. 8 shows that the low frame rate spectrum misses information, e.g. those from 40 to 150 Hz, that may be important for the diagnosis of diseases. Moreover, even for frequency lower than 40 Hz the spectrum is considerably attenuated, likely due to low-pass filtering, that may impact on actual diagnostic content of strain rate curves. Therefore, a frame rate up to 72 Hz seems to be too low for time resolved description of strain rate curves. On the other hand, the HFR spectrum also shows that it is unlikely to have important information at frequencies higher than 150 Hz for healthy heart, where the signal information is below the noise level. Hence, a frame rate of 300 Hz, rather than 957 Hz, could be sufficient for time resolved description of strain rate without significant information loss. However, since the current study only involved healthy volunteers, any conclusion on the useful frequency components should be deferred after clinical studies on patients, which may have important information at higher frequencies. Only after defining the optimal frame rate a different transmission scheme could be developed to improve the image quality and likely the accuracy of estimates.

Future work will include the development of different high frame rate transmission schemes and the investigation of different beamforming methods in reception, e.g. coherence based beamforming [54]–[56] that, by improving image quality, may improve the tracking as well. Moreover, a pilot clinical study will include the test on healthy subjects and heart failure with preserved ejection fraction (HfPEF) patients to determine if HFR imaging may allow a better diagnosis of that specific disease.

V. CONCLUSION

A novel speckle tracking algorithm for high frame rate imaging was introduced. The proposed estimator consists of a 2-step algorithm based on 1D cross-correlations to separately estimate the axial (using RF signals) and lateral displacement (using envelope data). It was first optimized and validated on simulated ultrasound data from 3D electromechanical models. Then, it was preliminary tested in-vivo on 10 healthy volunteers showing its clinical applicability and feasibility. It was shown that HFR-STE can obtain clinical markers in the same range as those reported in literature. Moreover, the estimated peak global longitudinal strain showed good correlation and negligible differences with that measured with a clinical scanner. Future work will include studies on diseased hearts (e.g. HfPEF) to determine if HFR imaging may allow a better diagnosis of specific diseases.

In conclusion, this paper illustrates that the time resolution of HFR imaging is too high to estimate the lateral displacement between consecutive frames, hence estimation should be performed on frames separated by a bigger time gap. In addition, since lateral motion estimates are mostly influenced by noise, it is suggested to use 2D kernels, even for 1D cross-correlation, which makes the speckle tracking less sensitive to noise.

Next developments will include the investigation of different beamforming methods in reception to improve image quality and hence the tracking.

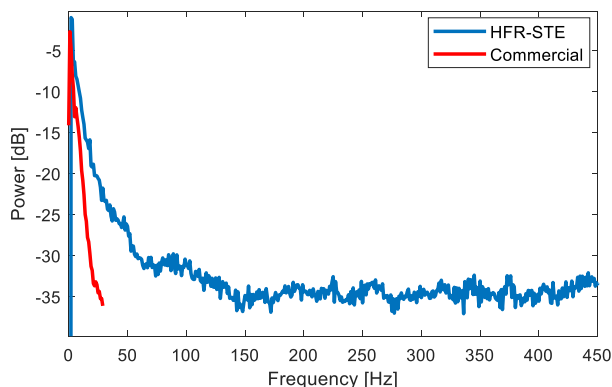


Fig. 8 Comparison between mean spectra of strain rates from all volunteers and all segments obtained with the commercial scanner and the proposed method (HFR-STE).

VI. REFERENCES

- [1] M. Davies *et al.*, "Prevalence of left-ventricular systolic dysfunction and heart failure in the Echocardiographic Heart of England Screening study: a population based study," *Lancet Lond. Engl.*, vol. 358, no. 9280, pp. 439–444, Aug. 2001.
- [2] F. Yousaf *et al.*, "Prevalence of left ventricular dysfunction in a UK community sample of very old people: the Newcastle 85+ study," *Heart Br. Card. Soc.*, vol. 98, no. 19, pp. 1418–1423, Oct. 2012, doi: 10.1136/heartjnl-2012-302457.
- [3] S. Urheim, T. Edvardsen, H. Torp, B. Angelsen, and O. A. Smiseth, "Myocardial strain by Doppler echocardiography. Validation of a new method to quantify regional myocardial function," *Circulation*, vol. 102, no. 10, pp. 1158–1164, Sep. 2000.
- [4] A. Stoylen, A. Heimdal, K. Bjornstad, H. G. Torp, and T. Skjaerpe, "Strain Rate Imaging by Ultrasound in the Diagnosis of Regional Dysfunction of the Left Ventricle," *Echocardiogr. Mt. Kisco N*, vol. 16, no. 4, pp. 321–329, May 1999.
- [5] M. Dandel, H. Lehmkuhl, C. Knosalla, N. Suramelashvili, and R. Hetzer, "Strain and strain rate imaging by echocardiography - basic concepts and clinical applicability," *Curr. Cardiol. Rev.*, vol. 5, no. 2, pp. 133–148, May 2009, doi: 10.2174/157340309788166642.
- [6] G. R. Sutherland *et al.*, "Color Doppler myocardial imaging: a new technique for the assessment of myocardial function," *J. Am. Soc. Echocardiogr. Off. Publ. Am. Soc. Echocardiogr.*, vol. 7, no. 5, pp. 441–458, Oct. 1994.
- [7] C.-M. Yu, J. E. Sanderson, T. H. Marwick, and J. K. Oh, "Tissue Doppler Imaging: A New Prognosticator for Cardiovascular Diseases," *J. Am. Coll. Cardiol.*, vol. 49, no. 19, pp. 1903–1914, May 2007, doi: 10.1016/j.jacc.2007.01.078.
- [8] W. N. McDicken, G. R. Sutherland, C. M. Moran, and L. N. Gordon, "Colour Doppler velocity imaging of the myocardium," *Ultrasound Med. Biol.*, vol. 18, no. 6–7, pp. 651–654, 1992.
- [9] A. Ramalli *et al.*, "Real-Time High-Frame-Rate Cardiac B-Mode and Tissue Doppler Imaging Based on Multiline Transmission and Multiline Acquisition," *IEEE Trans. Ultrason. Ferroelectr. Freq. Control*, vol. 65, no. 11, pp. 2030–2041, Nov. 2018, doi: 10.1109/TUFFC.2018.2869473.
- [10] J. J. Bax *et al.*, "Usefulness of myocardial tissue Doppler echocardiography to evaluate left ventricular dyssynchrony before and after biventricular pacing in patients with idiopathic dilated cardiomyopathy," *Am. J. Cardiol.*, vol. 91, no. 1, pp. 94–97, Jan. 2003.
- [11] D. Notabartolo *et al.*, "Usefulness of the peak velocity difference by tissue Doppler imaging technique as an effective predictor of response to cardiac resynchronization therapy," *Am. J. Cardiol.*, vol. 94, no. 6, pp. 817–820, Sep. 2004, doi: 10.1016/j.amjcard.2004.05.072.
- [12] R. O. Mada, J. Duchenne, and J.-U. Voigt, "Tissue Doppler, Strain and Strain Rate in ischemic heart disease 'How I do it,'" *Cardiovasc. Ultrasound*, vol. 12, no. 1, p. 38, Sep. 2014, doi: 10.1186/1476-7120-12-38.
- [13] A. J. Teske, B. W. L. De Boeck, P. G. Melman, G. T. Sieswerda, P. A. Doevendans, and M. J. M. Cramer, "Echocardiographic quantification of myocardial function using tissue deformation imaging, a guide to image acquisition and analysis using tissue Doppler and speckle tracking," *Cardiovasc. Ultrasound*, vol. 5, p. 27, Aug. 2007, doi: 10.1186/1476-7120-5-27.
- [14] J. D'hooge, "Principles and Different Techniques for Speckle Tracking," in *Myocardial Imaging: Tissue Doppler and Speckle Tracking*, John Wiley & Sons, Ltd, 2008, pp. 17–25.
- [15] D. Boukerroui, J. A. Noble, and M. Brady, "Velocity Estimation in Ultrasound Images: A Block Matching Approach," in *Information Processing in Medical Imaging*, 2003, pp. 586–598.
- [16] D. Adam *et al.*, "Ultrasonographic quantification of local cardiac dynamics by tracking real reflectors: algorithm development and experimental validation," in *Computers in Cardiology*, 2004, 2004, pp. 337–340, doi: 10.1109/CIC.2004.1442941.
- [17] S. Langeland *et al.*, "Experimental validation of a new ultrasound method for the simultaneous assessment of radial and longitudinal myocardial deformation independent of insonation angle," *Circulation*, vol. 112, no. 14, pp. 2157–2162, Oct. 2005, doi: 10.1161/CIRCULATIONAHA.105.554006.
- [18] I. Mikic, S. Krucinski, and J. D. Thomas, "Segmentation and tracking in echocardiographic sequences: active contours guided by optical flow estimates," *IEEE Trans. Med. Imaging*, vol. 17, no. 2, pp. 274–284, Apr. 1998, doi: 10.1109/42.700739.
- [19] E. D. Angelini and O. Gerard, "Review of Myocardial Motion Estimation Methods from Optical Flow Tracking on Ultrasound Data," in *2006 International Conference of the IEEE Engineering in Medicine and Biology Society*, 2006, pp. 1537–1540, doi: 10.1109/IEMBS.2006.259640.
- [20] M. J. Ledesma-Carbayo, P. Mahía-Casado, A. Santos, E. Pérez-David, M. A. García-Fernández, and M. Desco, "Cardiac motion analysis from ultrasound sequences using nonrigid registration: validation against Doppler tissue velocity," *Ultrasound Med. Biol.*, vol. 32, no. 4, pp. 483–490, Apr. 2006, doi: 10.1016/j.ultrasmedbio.2005.12.006.
- [21] B. Heyde *et al.*, "Regional cardiac motion and strain estimation in three-dimensional echocardiography: a validation study in thick-walled univentricular phantoms," *IEEE Trans. Ultrason. Ferroelectr. Freq. Control*, vol. 59, no. 4, pp. 668–682, Apr. 2012, doi: 10.1109/TUFFC.2012.2245.
- [22] B. Chakraborty, B. Heyde, M. Alessandrini, and J. D'hooge, "Fast myocardial strain estimation from 3D ultrasound through elastic image registration with analytic regularization," in *Medical Imaging 2016: Ultrasonic Imaging and Tomography*, 2016, vol. 9790, p. 979006, doi: 10.1117/12.2216781.
- [23] J.-U. Voigt *et al.*, "Definitions for a common standard for 2D speckle tracking echocardiography: consensus document of the EACVI/ASE/Industry Task Force to standardize deformation imaging," *Eur. Heart J. Cardiovasc. Imaging*, vol. 16, no. 1, pp. 1–11, Jan. 2015, doi: 10.1093/ehjci/jeu184.
- [24] J. D'hooge *et al.*, "Regional strain and strain rate measurements by cardiac ultrasound: principles, implementation and limitations," *Eur. J. Echocardiogr. J. Work. Group Echocardiogr. Eur. Soc. Cardiol.*, vol. 1, no. 3, pp. 154–170, Sep. 2000, doi: 10.1053/euje.2000.0031.
- [25] N. L. Greenberg *et al.*, "Doppler-derived myocardial systolic strain rate is a strong index of left ventricular contractility," *Circulation*, vol. 105, no. 1, pp. 99–105, Jan. 2002.
- [26] M. Bauer *et al.*, "Echocardiographic speckle-tracking based strain imaging for rapid cardiovascular phenotyping in mice," *Circ. Res.*, vol. 108, no. 8, pp. 908–916, Apr. 2011, doi: 10.1161/CIRCRESAHA.110.239574.
- [27] R. Mallart and M. Fink, "Improved imaging rate through simultaneous transmission of several ultrasound beams," in *New Developments in Ultrasonic Transducers and Transducer Systems*, 1992, vol. 1733, pp. 120–131, doi: 10.1117/12.130591.
- [28] L. Tong, H. Gao, and J. D'hooge, "Multi-transmit beam forming for fast cardiac imaging—a simulation study," *IEEE Trans. Ultrason. Ferroelectr. Freq. Control*, vol. 60, no. 8, pp. 1719–1731, Aug. 2013, doi: 10.1109/TUFFC.2013.2753.
- [29] L. Tong, A. Ramalli, R. Jasaityte, P. Tortoli, and J. D'hooge, "Multi-Transmit Beam Forming for Fast Cardiac Imaging—Experimental Validation and In Vivo Application," *IEEE Trans. Med. Imaging*, vol. 33, no. 6, pp. 1205–1219, Jun. 2014, doi: 10.1109/TMI.2014.2302312.
- [30] G. Matrone, A. Ramalli, A. S. Savoia, P. Tortoli, and G. Magenes, "High Frame-Rate, High Resolution Ultrasound Imaging With Multi-Line Transmission and Filtered-Delay Multiply And Sum Beamforming," *IEEE Trans. Med. Imaging*, vol. 36, no. 2, pp. 478–486, 2017, doi: 10.1109/TMI.2016.2615069.
- [31] F. Prieur, B. Dénarié, A. Austeng, and H. Torp, "Multi-line transmission in medical imaging using the second-harmonic signal," *IEEE Trans. Ultrason. Ferroelectr. Freq. Control*, vol. 60, no. 12, pp. 2682–2692, Dec. 2013, doi: 10.1109/TUFFC.2013.2868.
- [32] M. Tanter and M. Fink, "Ultrafast imaging in biomedical ultrasound," *IEEE Trans. Ultrason. Ferroelectr. Freq. Control*, vol. 61, no. 1, pp. 102–119, Jan. 2014, doi: 10.1109/TUFFC.2014.6689779.
- [33] B. Denarie *et al.*, "Coherent plane wave compounding for very high frame rate ultrasonography of rapidly moving targets," *IEEE Trans. Med. Imaging*, vol. 32, no. 7, pp. 1265–1276, Jul. 2013, doi: 10.1109/TMI.2013.2255310.
- [34] H. Hasegawa and H. Kanai, "High-frame-rate echocardiography using diverging transmit beams and parallel receive beamforming," *J. Med. Ultrason. 2001*, vol. 38, no. 3, pp. 129–140, Jul. 2011, doi: 10.1007/s10396-011-0304-0.
- [35] C. Papadacci, M. Pernot, M. Couade, M. Fink, and M. Tanter, "High-contrast ultrafast imaging of the heart," *IEEE Trans. Ultrason. Ferroelectr. Freq. Control*, vol. 61, no. 2, pp. 288–301, Feb. 2014, doi: 10.1109/TUFFC.2014.6722614.
- [36] J. Grondin, V. Ssayseng, and E. E. Konofagou, "Cardiac Strain Imaging With Coherent Compounding of Diverging Waves," *IEEE Trans. Ultrason. Ferroelectr. Freq. Control*, vol. 64, no. 8, pp. 1212–1222, Aug. 2017, doi: 10.1109/TUFFC.2017.2717792.
- [37] P. Joos *et al.*, "High-Frame-Rate Speckle-Tracking Echocardiography," *IEEE Trans. Ultrason. Ferroelectr. Freq. Control*, vol. 65, no. 5, pp. 720–728, 2018, doi: 10.1109/TUFFC.2018.2809553.
- [38] J. Poree, D. Posada, A. Hodzic, F. Tournoux, G. Cloutier, and D. Garcia, "High-Frame-Rate Echocardiography Using Coherent Compounding With Doppler-Based Motion-Compensation," *IEEE Trans. Med. Imaging*, vol. 35, no. 7, pp. 1647–1657, Jul. 2016, doi: 10.1109/TMI.2016.2523346.

- [39] V. Komini, P. Santos, and J. D'hooge, "Diverging wave compounding: Direct comparison of two popular approaches," in *2017 IEEE International Ultrasonics Symposium (IUS)*, 2017, pp. 1–4, doi: 10.1109/ULTSYM.2017.8092802.
- [40] J. A. Jensen and N. B. Svendsen, "Calculation of pressure fields from arbitrarily shaped, apodized, and excited ultrasound transducers," *IEEE Trans. Ultrason. Ferroelectr. Freq. Control*, vol. 39, no. 2, pp. 262–267, Mar. 1992, doi: 10.1109/58.139123.
- [41] J. A. Jensen, "FIELD: A Program for Simulating Ultrasound Systems," in *10th Nordicaltic Conference on Biomedical Imaging, Vol. 4, Supplement 1, Part 1:351–353*, 1996, pp. 351–353.
- [42] M. Alessandrini *et al.*, "A Pipeline for the Generation of Realistic 3D Synthetic Echocardiographic Sequences: Methodology and Open-Access Database," *IEEE Trans. Med. Imaging*, vol. 34, no. 7, pp. 1436–1451, Jul. 2015, doi: 10.1109/TMI.2015.2396632.
- [43] A. Ortega *et al.*, "HD-PULSE: High channel Density Programmable ULtrasound System based on consumer Electronics," in *2015 IEEE International Ultrasonics Symposium (IUS)*, 2015, pp. 1–3, doi: 10.1109/ULTSYM.2015.0516.
- [44] H. Li, Y. Guo, and W.-N. Lee, "Systematic Performance Evaluation of a Cross-Correlation-Based Ultrasound Strain Imaging Method," *Ultrasound Med. Biol.*, vol. 42, no. 10, pp. 2436–2456, Oct. 2016, doi: 10.1016/j.ultrasmedbio.2016.06.015.
- [45] J. Pedrosa *et al.*, "Fast and Fully Automatic Left Ventricular Segmentation and Tracking in Echocardiography Using Shape-Based B-Spline Explicit Active Surfaces," *IEEE Trans. Med. Imaging*, vol. 36, no. 11, pp. 2287–2296, Nov. 2017, doi: 10.1109/TMI.2017.2734959.
- [46] A. Savitzky and M. Golay, "Smoothing and Differentiation of Data by Simplified Least Squares Procedures," *Anal. Chem.*, vol. 36, pp. 1627–1639, Jul. 1964, doi: 10.1021/ac60214a047.
- [47] J.-U. Voigt *et al.*, "Assessment of Regional Longitudinal Myocardial Strain Rate Derived from Doppler Myocardial Imaging Indexes in Normal and Infarcted Myocardium," *J. Am. Soc. Echocardiogr.*, vol. 13, no. 6, pp. 588–598, Jun. 2000, doi: 10.1067/mje.2000.105631.
- [48] B. S. Ramamurthy and G. E. Trahey, "Potential and limitations of angle-independent flow detection algorithms using radio-frequency and detected echo signals," *Ultrason. Imaging*, vol. 13, no. 3, pp. 252–268, Jul. 1991, doi: 10.1016/0161-7346(91)90075-S.
- [49] L. N. Bohs, B. J. Geiman, M. E. Anderson, S. C. Gebhart, and G. E. Trahey, "Speckle tracking for multi-dimensional flow estimation," *Ultrasonics*, vol. 38, no. 1–8, pp. 369–375, Mar. 2000.
- [50] T. H. Marwick *et al.*, "Myocardial Strain Measurement With 2-Dimensional Speckle-Tracking Echocardiography: Definition of Normal Range," *JACC Cardiovasc. Imaging*, vol. 2, no. 1, pp. 80–84, Jan. 2009, doi: 10.1016/j.jcmg.2007.12.007.
- [51] O. Mirea *et al.*, "Variability and Reproducibility of Segmental Longitudinal Strain Measurement: A Report From the EACVI-ASE Strain Standardization Task Force," *JACC Cardiovasc. Imaging*, vol. 11, no. 1, pp. 15–24, 2018, doi: 10.1016/j.jcmg.2017.01.027.
- [52] A. Fatemi, E. A. R. Berg, and A. Rodriguez-Molares, "Studying the Origin of Reverberation Clutter in Echocardiography: In Vitro Experiments and In Vivo Demonstrations," *Ultrasound Med. Biol.*, Apr. 2019, doi: 10.1016/j.ultrasmedbio.2019.01.010.
- [53] B. E. Treeby and B. T. Cox, "k-Wave: MATLAB toolbox for the simulation and reconstruction of photoacoustic wave fields," *J. Biomed. Opt.*, vol. 15, no. 2, p. 021314, Mar. 2010, doi: 10.1117/1.3360308.
- [54] Pai-Chi Li and Meng-Lin Li, "Adaptive imaging using the generalized coherence factor," *IEEE Trans. Ultrason. Ferroelectr. Freq. Control*, vol. 50, no. 2, pp. 128–141, Feb. 2003, doi: 10.1109/TUFFC.2003.1182117.
- [55] J. Camacho, M. Parrilla, and C. Fritsch, "Phase Coherence Imaging," *IEEE Trans. Ultrason. Ferroelectr. Freq. Control*, vol. 56, no. 5, pp. 958–974, May 2009, doi: 10.1109/TUFFC.2009.1128.
- [56] G. Matrone and A. Ramalli, "Spatial Coherence of Backscattered Signals in Multi-Line Transmit Ultrasound Imaging and Its Effect on Short-Lag Filtered-Delay Multiply and Sum Beamforming," *Appl. Sci.*, vol. 8, no. 4, p. 486, Apr. 2018, doi: 10.3390/app8040486.